Initial observations with the Global Ultraviolet Imager (GUVI) in the NASA TIMED satellite mission

A. B. Christensen,[1] L. J. Paxton,[2] S. Avery,[3] J. Craven,[4] G. Crowley,[5] D. C. Humm,[2] H. Kil,[2] R. R. Meier,[6] C.-I. Meng,[2] D. Morrison,[2] B. S. Ogorzalek,[2] P. Straus,[1] D. J. Strickland,[7] R. M. Swenson,[8] R. L. Walterscheid,[1] B. Wolven,[2] and Y. Zhang[2]

Received 1 March 2003; revised 21 August 2003; accepted 3 October 2003; published 23 December 2003.

[1] The Global Ultraviolet Imager (GUVI) instrument carried aboard the NASA TIMED satellite measures the spectral radiance of the Earth's far ultraviolet airglow in the spectral region from 120 to 180 nm using a cross-track scanning spectrometer design. Continuous operation of the instrument provides images of the Earth's disk and limb in five selectable spectral bands. Also, spectra at fixed scanning mirror position can be obtained. Initial results demonstrate the quantitative functionality of the instrument for studies of the Earth's dayglow, aurora, and ionosphere. Moreover, through forward modeling, the abundance of the major constituents of the thermosphere, O, N_2, and O_2 and thermospheric temperatures can be retrieved from observations of the limb radiance. Variations of the column O/N_2 ratio can be deduced from sunlit disk observations. In regions of auroral precipitation not only can the aurora regions be geographically located and the auroral boundaries identified, but also the energy flux Q, the characteristic energy E_o, and a parameter f_o that scales the abundance of neutral atomic oxygen can be derived. Radiance due to radiative recombination in the ionospheric F region is evident from both dayside and nightside observations of the Earth's limb and disk, respectively. Regions of depleted F-region electron density are evident in the tropical Appleton anomaly regions, associated with so-called ionospheric "bubbles." Access to the GUVI data is provided through the GUVI website www.timed.jhuapl.edu\guvi. *INDEX TERMS:* 0310 Atmospheric Composition and Structure: Airglow and aurora; 0355 Atmospheric Composition and Structure: Thermosphere—composition and chemistry; 0358 Atmospheric Composition and Structure: Thermosphere—energy deposition; 2407 Ionosphere: Auroral ionosphere (2704); *KEYWORDS:* airglow, aurora, ultraviolet, imaging, satellite, atmosphere

Citation: Christensen, A. B., et al., Initial observations with the Global Ultraviolet Imager (GUVI) in the NASA TIMED satellite mission, *J. Geophys. Res.*, *108*(A12), 1451, doi:10.1029/2003JA009918, 2003.

1. Introduction

[2] The Global Ultraviolet Imager (GUVI) is one of four scientific instruments aboard the NASA TIMED (Thermosphere Ionosphere Mesosphere Energy and Dynamics) satellite launched from Vandenberg, California on 7 December 2001 into a 630-km, 97.8-min period, circular polar orbit with an inclination of 74.1°. The TIMED mission is to investigate and understand the energetics of the mesosphere and lower thermosphere with an emphasis on the altitude region from 60 to 180 km. The mission seeks to determine the temperature, density, composition, and wind structure, including seasonal and latitudinal variations, and to investigate the relative importance of the various radiative, chemical, electrodynamical, and dynamical sources and sinks of energy that influence the thermal structure of the region. The payload comprises the SABER (Sounding of the Atmosphere using Broadband Emission Radiometry) instrument [*Russell et al.*, 1999] for sensing minor constituent atmospheric gasses, TIDI (TIMED Doppler Interferometer) [*Killeen et al.*, 1999] for measurement of wind speed and direction, SEE (Solar Extreme Ultraviolet Experiment) [*Woods et al.*, 1998] for monitoring the solar ultraviolet irradiance, and GUVI [*Christensen et al.*, 1994] for imaging the Earth's far ultraviolet (FUV) airglow.

[3] The GUVI scientific investigation makes spectroradiometric measurements of the far ultraviolet (FUV) airglow emission. The primary far ultraviolet spectral features are due to the major constituents of the upper atmosphere, namely H, O, and N_2 in emission and O_2 in absorption [c.f. *Meier*, 1991, and references therein]. The spectrum has

[1]Space Science Applications Laboratory, Aerospace Corporation, El Segundo, California, USA.
[2]Applied Physics Laboratory, Johns Hopkins University, Laurel, Maryland, USA.
[3]University of Colorado, Boulder, Colorado, USA.
[4]University of Alaska, Fairbanks, Alaska, USA.
[5]Southwest Research Institute, San Antonio, Texas, USA.
[6]E.O. Hulburt Center for Space Research, Naval Research Laboratory, Washington D.C., USA.
[7]Computational Physics, Inc, Springfield, Virginia, USA.
[8]Utah State University, Logan, Utah, USA.

0148-0227/03/2003JA009918$09.00

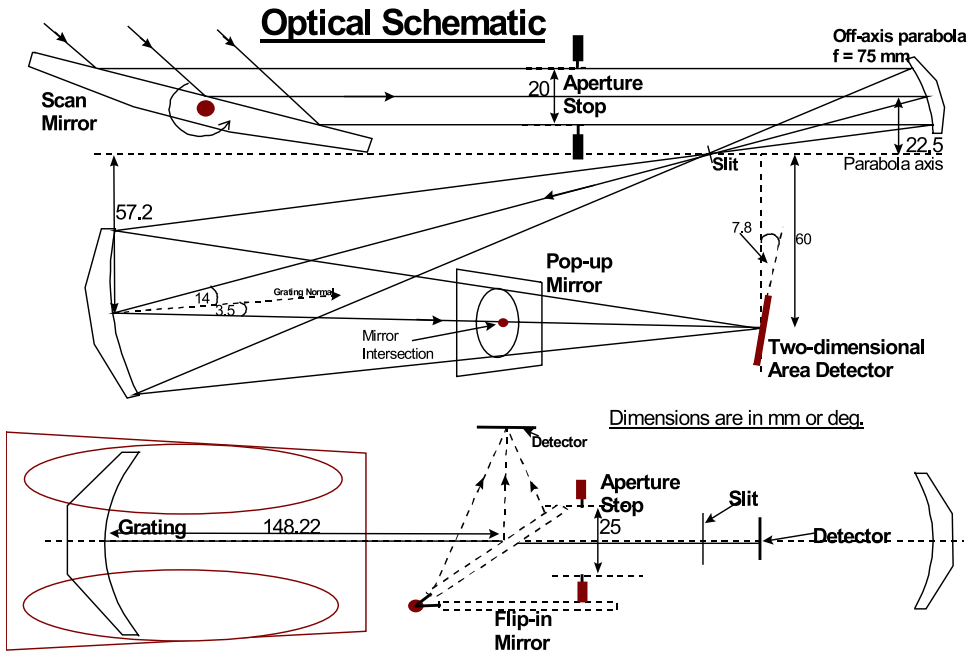

Figure 1. Side and top view optical schematics of the GUVI spectrograph.

been well characterized through satellite and rocket experiments [c.f., *Huffman et al.*, 1980; *Feldman and Gentieu*, 1982; *Eastes et al.*, 1985; *Meier et al.*, 1985]. The spatial distributions and temporal variations of the major species in the altitude range from approximately 130 to 400 km in the thermosphere can be derived from the radiances of the FUV spectral features in the sunlit atmosphere [c.f. *Strickland and Thomas*, 1976; *Meier and Anderson*, 1983; *Meier et al.*, 1985; *Meier*, 1991; *Strickland et al.*, 1995; *Craven et al.*, 1994; *Immel et al.*, 2001].

[4] The FUV can also be used to infer the solar energy input ($\lambda < 40$ nm) [*Strickland et al.*, 1995], determine characteristics of auroral particles that deposit energy in the thermosphere [c.f. *Strickland et al.*, 1983; *Germany et al.*, 1994; *Lummerzheim et al.*, 1991], and observe properties of the ionospheric F region [e.g., *Dymond et al.*, 1997].

[5] The GUVI instrument operates continually throughout each TIMED orbit and registers the radiance of FUV emissions from the upper atmosphere. A rotating mirror scans the instantaneous field-of-view of the entrance slit on the GUVI spectrograph across the Earth's limb and disk. The radiance measured in five bandpass channels, selected to capture the primary emission features of H, O, and N_2, comprises the basic measured quantities. A set of algorithms are used to derive the principal products of the GUVI investigation including neutral density profiles and abundances, temperatures, integrated ionizing solar flux and variables related to auroral precipitation. This paper presents initial images of the FUV airglow and early results of the GUVI investigation.

2. Instrument Description

[6] The GUVI instrument subsystems include an imaging spectrograph, a scanning mechanism, a detector system, and data handling and control electronics. A cross-track scanning technique provides airglow images of the Earth in five wavelength channels between 115 and 180 nm. Major emission features within those channels include H (121.6), OI(130.4), OI(135.6), and the N_2 LBH bands. Up to five spectral bands can be observed simultaneously.

[7] The GUVI spectrograph [*Humm et al.*, 1998; *Paxton et al.*, 1998; *Humm et al.*, 1999; *Paxton et al.*, 1999; *Morrison et al.*, 2002] is based on the design for the Defense Meteorological Satellite Program (DMSP) Special Sensor Ultraviolet Spectrographic Imager (SSUSI) [*Paxton et al.*, 1992a, 1992b; *Paxton et al.*, 2002]. It is a Roland circle mount with an f/3, 0.215-m focal length concave, spherical toroidal holographic grating ruled at 1200 grooves/mm. A schematic of the optical layout is provided in Figure 1. Light reflected from the scan mirror is imaged on the slit by a superpolished fore optic (f = 75 mm). Three open slit widths are selectable for the narrow, medium, and wide configurations: 0.24, 0.39, and

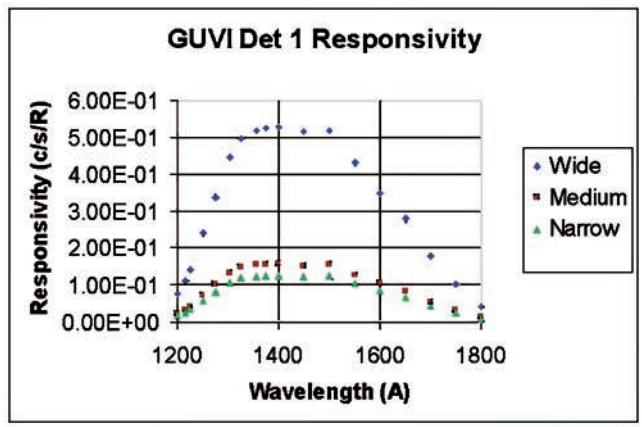

Figure 2. The GUVI responsivity in sensor counts/s/R/pixel for the three open slit configurations.

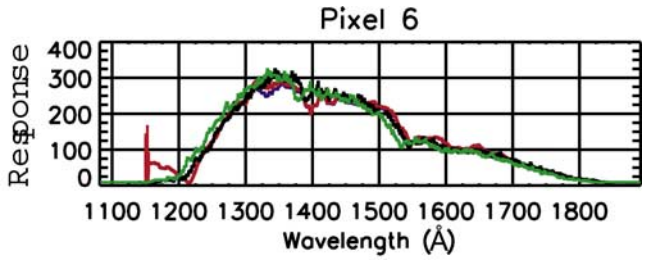

Figure 3. Stellar responsivity calibration data collected on 7 April 2002 (Day 97) (red) and IUE spectrum for star HV 5953 (black line).

0.97 mm, respectively. (For reference, GUVI software and documentation identifies the slit widths as 3, 2, and 1, respectively, with 0 for the closed position.) The instrument has two focal plane detector heads accessed optically using a movable folding mirror. Both are based on the wedge-and-strip photon counting and location concept [*Martin et al.*, 1981] and are described in detail by *Goldsten et al.* [1999].

[8] The responsivity R of the full system as a function of wavelength based on laboratory measurements obtained prior to flight [*Humm et al.*, 1999] is shown in Figure 2. It is limited to ray paths along a central region of the focal plane. The short wavelength cutoff at 120 nm is due to the window material (magnesium fluoride). The long-wavelength responsivity is limited by the photocathode quantum efficiency. Variations in response with position for other ray paths were also measured during the laboratory calibration to create a flat-fielding algorithm that is applied to the all raw detector response rates. The data reduction procedure also takes into account variations in reflectance of the scan mirror with angle of incidence and with location on its surface.

[9] Repeated observation of UV-bright stars is used to verify and monitor the responsivity of the instrument during the flight mission. The first stellar calibration event occurred on 7 April (day 97) 2002, approximately 4 months after launch, and continues as an ongoing mission activity. Figure 3 compares the GUVI measured irradiance to the International Ultraviolet Explorer irradiance for one of several pixels that captured the star HV5953. Since the trajectory of a star across the focal plane is an arc, not all pixels are illuminated with each stellar observation. The responsivity of the instrument on the basis of this in-flight calibration at 135 nm was $R_{inflight} = 0.104 \pm 0.015$. The corresponding preflight laboratory value was $R_{preflight} = 0.094 \pm 0.007$.

[10] Stars are also used to verify the pointing accuracy of the instrument including the orientation of the satellite. The absolute pointing error along the GUVI line of sight with respect to an Earth-centered inertial reference frame is less than 0.05 degrees. Individual pixels are located to within ±0.05 degrees when all known sources of uncertainty in the attitude determination are included.

[11] The diagram in Figure 4 shows the basic elements of the scan geometry. The mirror can be held in a fixed position or scanned back and forth across the disk and limb. In the imaging mode, the scan-mirror subsystem [*Humm et al.*, 1998] scans the instantaneous field-of-view transverse to the ground track (cross-track) of the satellite once every 15 s. The scan always begins on the limb and consists of 191 steps (32 on the limb and 159 on the disk) covering 140 degrees, i.e., 80 degrees from nadir and above the limb on the cold side of the satellite (away from the Sun) to 60 degrees on the disk toward the warm side. On the limb, the scan mirror is incremented by 0.40 degrees every 0.068 s. However, detector count data are only accumulated for the final 0.034 s to allow time for the mirror motion damping. The disk steps are also 0.40 degrees, however, the

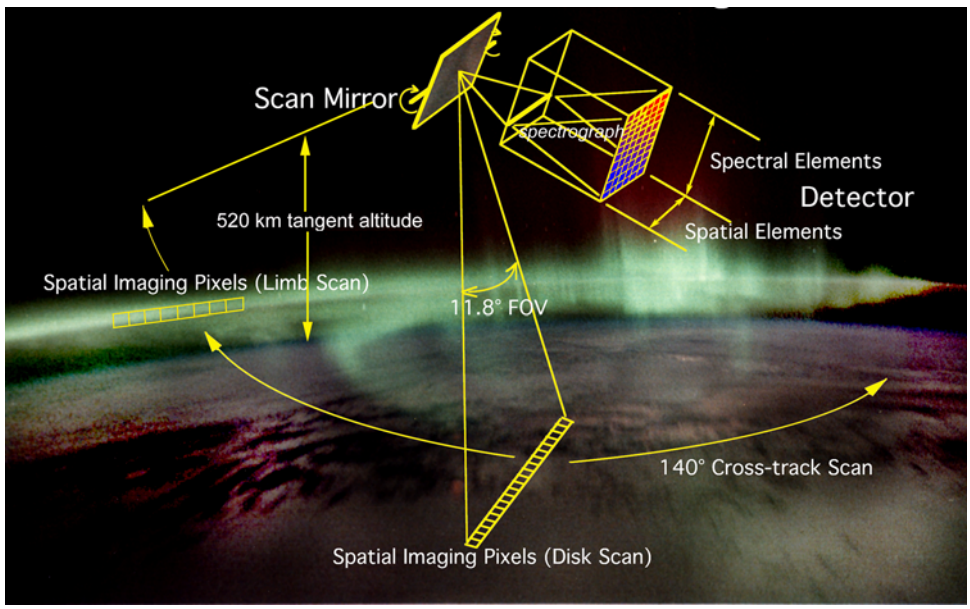

Figure 4. Illustration of the scan operation of the GUVI instrument. The slit dimension is projected along the ground track of the satellite and is subdivided into 14 pixels. The cross track scan is initiated every 15 s.

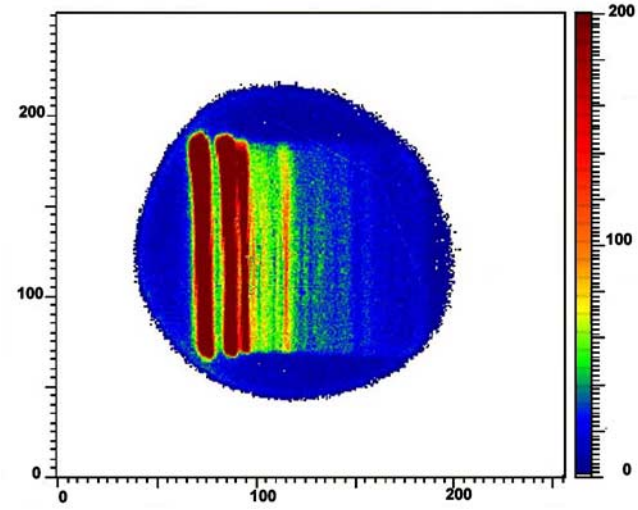

Figure 5. Example on-orbit data from the focal plane detector (Photek Detector). This figure represents the distribution of photon detection events on the focal plane collected during an observation of the Earth's FUV airglow. The along-slit spatial dimension is in the vertical. It is divided into 14 pixels. The spectral dimension is in the horizontal and is divided into 174 pixels. In the spectrographic mode a focal plane image is collected every 3.0 s and the full image relayed to the ground. In the imaging mode, the focal plane image is collected every dwell period, e.g., 62 ms on the disk, and only the pixels defined by the onboard "color" table are relayed to the ground. The bright emission lines from left to right are H(Lyα), OI(130.4), and OI(135.6) followed by N_2 LBH bands and N lines. The image has been rotated and corrected for distortion.

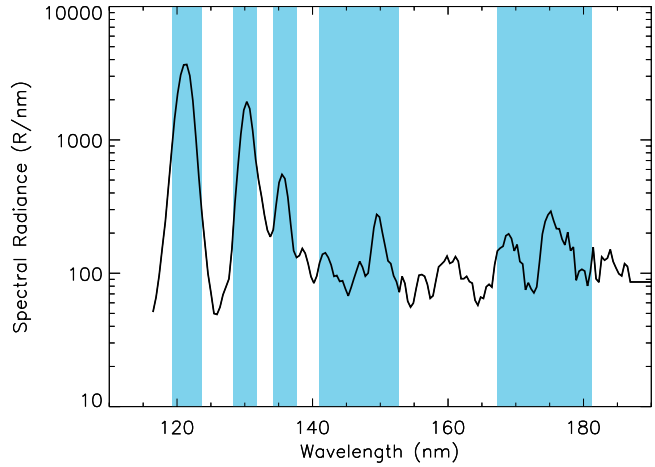

Figure 6. An auroral spectrum with the channel passbands identified. The photon counts from five wavelength regions are accumulated and sent via telemetry to the ground. The blue shaded bands identify the passbands of the standard channels. Although the dominant emitting species identifies the channels, other weaker emitters may contribute to the total count response. The atomic lines of H (Lyα), OI (130.4), and OI (135.6) are included in the three short wavelength channels, respectively. Two channels cover portions of the of LBH bands, LBHS and LBHL.

motor is stepped twice (total 0.8 degrees) during each 0.068 s and the count data are accumulated for 0.064 s of the 0.068s period.

[12] The image of the slit at the focal plane is divided into 14 spatial pixels, each subtending approximately 0.85 degrees along the length of the slit. The cross-track dimension is dependent on the slit width. For the narrow slit, the instantaneous cross-track dimension is approximately 0.2 degrees. However, since the mirror is moving almost continuously in the disk-scanning mode, the effective width is approximately 0.8 degrees, resulting in an approximate 7 $\times$ 7-km pixel dimension in the nadir when projected to 150-km altitude.

[13] At the focal plane of the spectrograph, the detector records the position of each photon event. The distribution of events is illustrated in Figure 5. The along-slit length is divided into 14 pixels, and the spectral dimension is divided into 176 pixels, each covering approximately 0.4 nm. The distortions present in the focal plane image are corrected in the ground processing software.

[14] In the spectrographic mode, the scan mirror remains fixed in a selectable position, generally chosen as the nadir position, and the full content of the focal plane accumulator array is transferred via telemetry to the ground. The accumulation dwell period is 3.0 s. The primary motivation for collecting Spectrograph Mode data on GUVI is to check the operation of the instrument, monitor the scattered light performance, and verify the consistency of airglow radiances measured in the imaging mode.

[15] In the imaging mode, only the photon counting events from five selectable spectral regions of the focal plane are accumulated at each scan-mirror position and recorded and transferred to the ground via telemetry. The standard channels are indicated in Figure 6, superimposed on a representative GUVI on-orbit auroral spectrum. Table 1 lists the passbands for the channels for the narrow (standard) slit position. Note also that the OI (135.6) channel in the dayglow and aurora contains a contribution from N_2 LBH emission.

[16] The counting rate is corrected during processing for both in-band and out-of-band scattered light. The former comes primarily from scattering on the grating and the later from light at longer wavelengths where there is still some detector response (i.e., "red" leak). During daylight the corrections for the "atomic" channels are small. Because of the large Rayleigh scattered background, the dayside disk observations for the LBH channels must be corrected. The scattered light from all sources amounts to approximately 20% in the LBHS increasing to approximately 30% of the

Table 1. Passbands of the Standard GUVI Channels Using the Narrow Slit

Channel	Passband	Emission
H (121.6)	119.3–123.6	HI (121.6)
O (130.4)	128.3–131.8	OI(130.4)
O (135.6)	134.3–137.7	OI(135.6) and N_2(LBH)
LBHS	141.0–152.8 nm	N_2(LBH) and NI(149.3)
LBHL	167.2–181.2 nm	N_2(LBH), NI (174.3), and N_2 VK

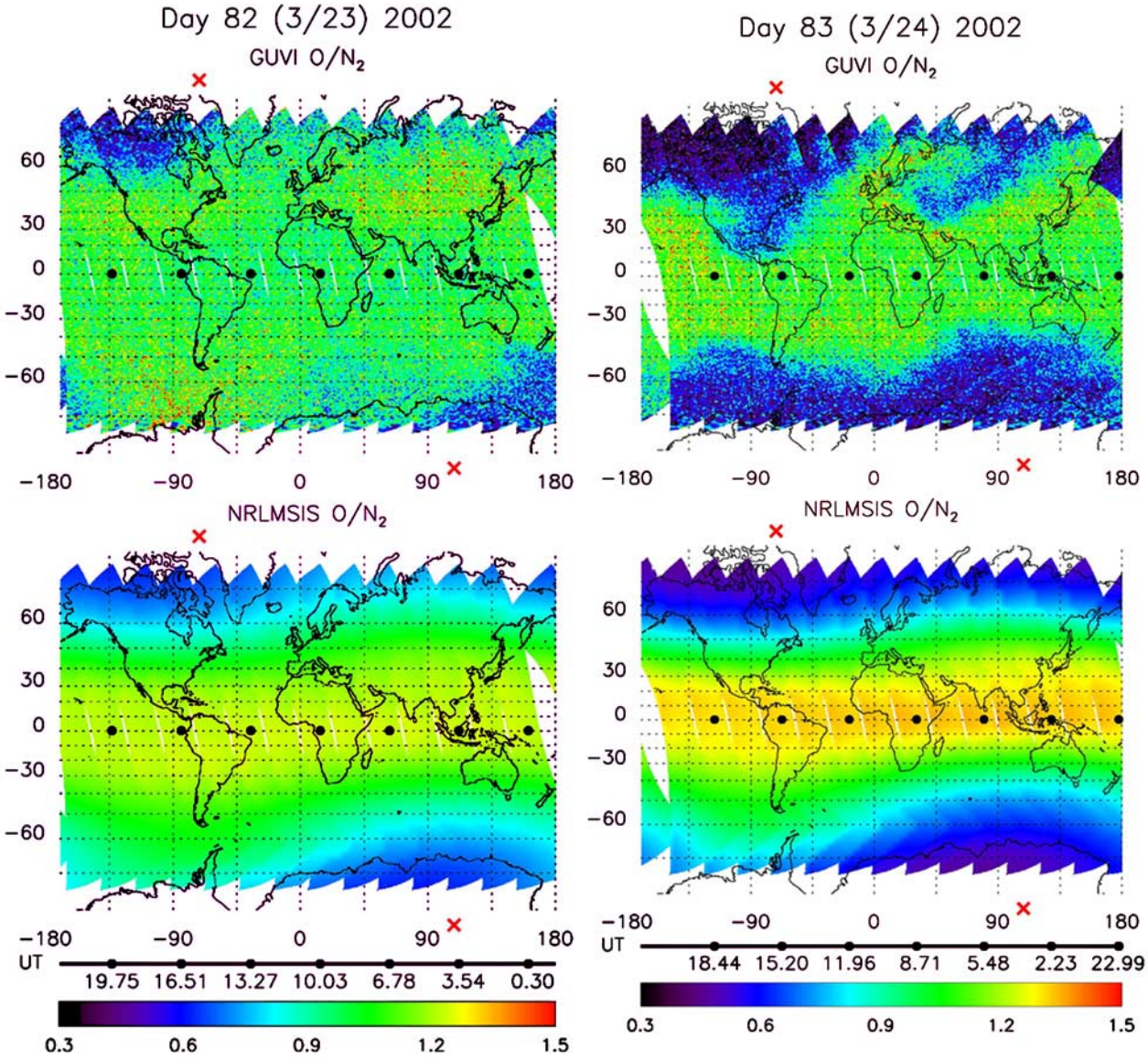

Figure 7. An overlay of successive dayside orbits on 23–24 (day 82–83) March 2002 (upper panels), showing the column O/N_2 ratio derived from the GUVI radiance measurements. The data cover a full 24 hours of the day at a fixed local time as the Earth rotates under the TIMED orbit. The local solar time for each equatorial crossing was 1200 noon (lower panels). The NRLMSIS-00 model values for the same days and same locations as the GUVI observations. The time scales serve to illustrate that 24 hours of observations were used to produce the GUVI images. The dots on the scales identify selected times at which the satellite crossed the equator. The locations of the satellite at these times are shown by the dots in the images.

total count rate in the LBHL channel. The corrections for limb viewing are only important at high altitudes (note Figure 5).

3. Observations

3.1. Composition From Dayglow Disk Imaging

[17] We have chosen data from 23 and 24 March (days 82–83) 2002 to illustrate the global behavior of the column O/N_2 ratio derived from the GUVI data (Figure 7). These days span the transition from relatively quiet to geomagnetically disturbed conditions. Day 82 began with a Kp value of 0, which rose to 3.5 at midday, and reached 5 at the end of the day. On day 83, Kp reached 6 in the first 6 hours and then fell to about 2 at day's end.

[18] To derive the column O/N_2 composition ratio, we used the dayglow algorithm of D. J. Strickland (Dayglow and auroral remote sensing algorithms for TIMED/GUVI, submitted to *Journal of Geophysical Research*, 2003, hereinafter referred to as Strickland, submitted manuscript, 2003) for specific application to GUVI. The algorithm makes use of the O (135.6) and LBHS channel data for disk viewing (-60° sunward side of orbit to $+62^\circ$ antisunward). Strickland (submitted manuscript, 2003) provides details about the

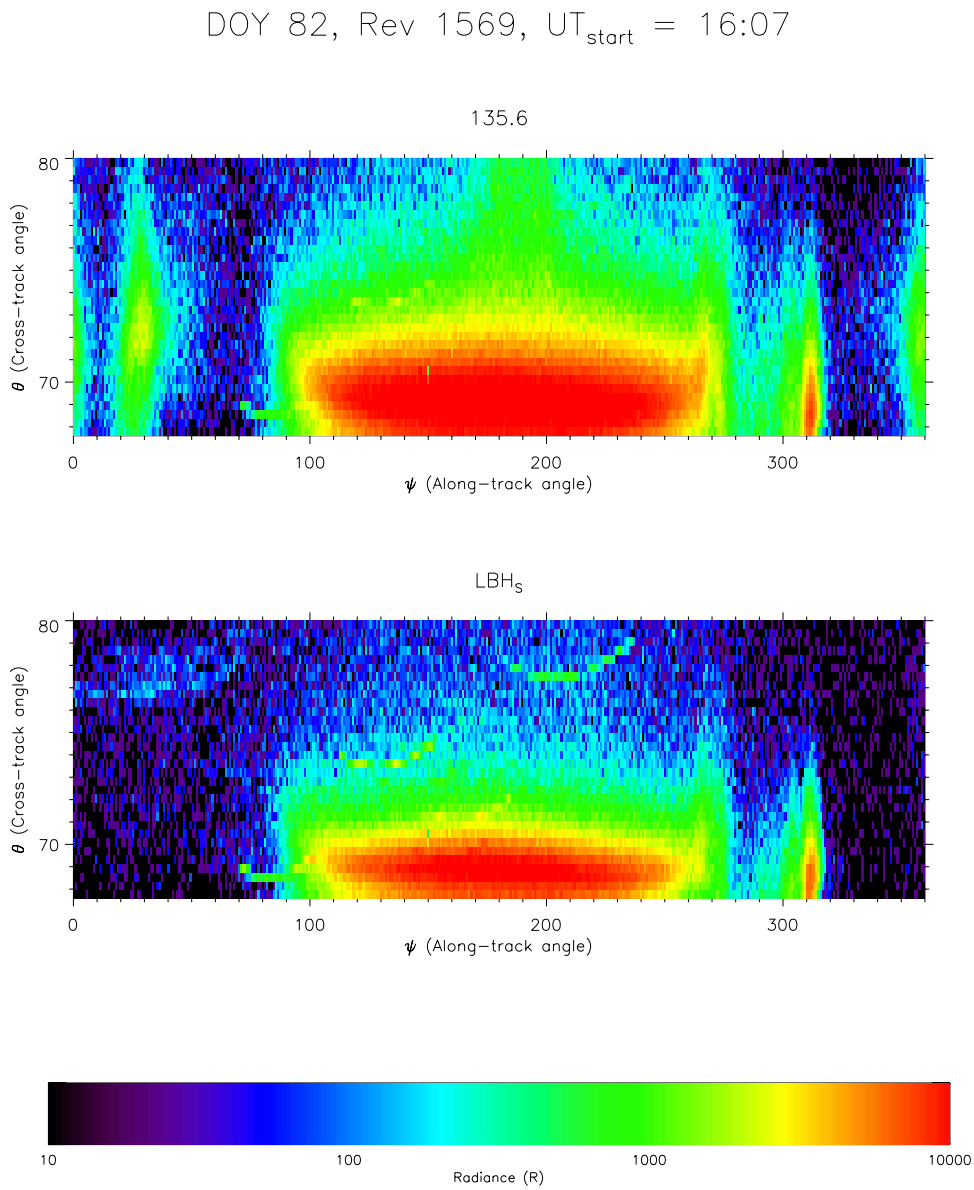

Figure 8. Full orbit GUVI image data for limb scans for O (135.6) channel (upper panel) and LBHS channel (lower panel). "U-shaped" streaks are caused by stars.

sources of emission contributing to these channels. We used Lookup Table 2 from Strickland (submitted manuscript, 2003) for which the N_2 LBH cross section of *Ajello and Shemansky* [1985] has been scaled by 1.4. *Eastes* [2000] and J. Ajello (private communication, 2001) have recommended that this cross section be increased due to cascading from the a' and w states of N_2 that is unaccounted for in present algorithm. A factor as high as 1.6 was recommended in the Eastes paper (taking into consideration radiative and collisional cascading). A preliminary analysis by the authors comparing O/N_2 ratios derived from GUVI limb and disk observations supports an increase to 1.4 (D. J. Strickland et al., Quiet-tie seasonal behavior of the thermosphere seen in the far ultraviolet dayglow, submitted to *Journal of Geophysical Research*, 2003). The impact of errors in the cross section, and more specifically of relative errors in cross sections between the 135.6 and the LBH channels, creates a bias in derived O/N_2. While some bias is unavoidable due to cross section uncertainties, relative variations in O/N_2 derived from GUVI data are unaffected by them.

[19] Figure 7 shows the GUVI derived O/N_2 and that predicted by the NRLMSIS-00 model [*Picone et al.*, 2002] on the days of interest (NRLMSISE-00 is the latest version of the MSIS empirical atmospheric model.) Data from 14 contiguous passes are used for each of these days. It is emphasised that each image spans almost 24 hours in UT but that the local time is the same for each orbit (near noon at the equator). The saw-tooth patterns at the top and bottom of each figure reflect scan cutoffs near 60°N and 60°S. The column O/N_2 ratio from the first orbit of the day appears to the left of the blank space that is present due to limiting the displays to the above-mentioned 14 passes. The region of reduced O/N_2 over and eastward of South America should be ignored, since observations in this region are contami-

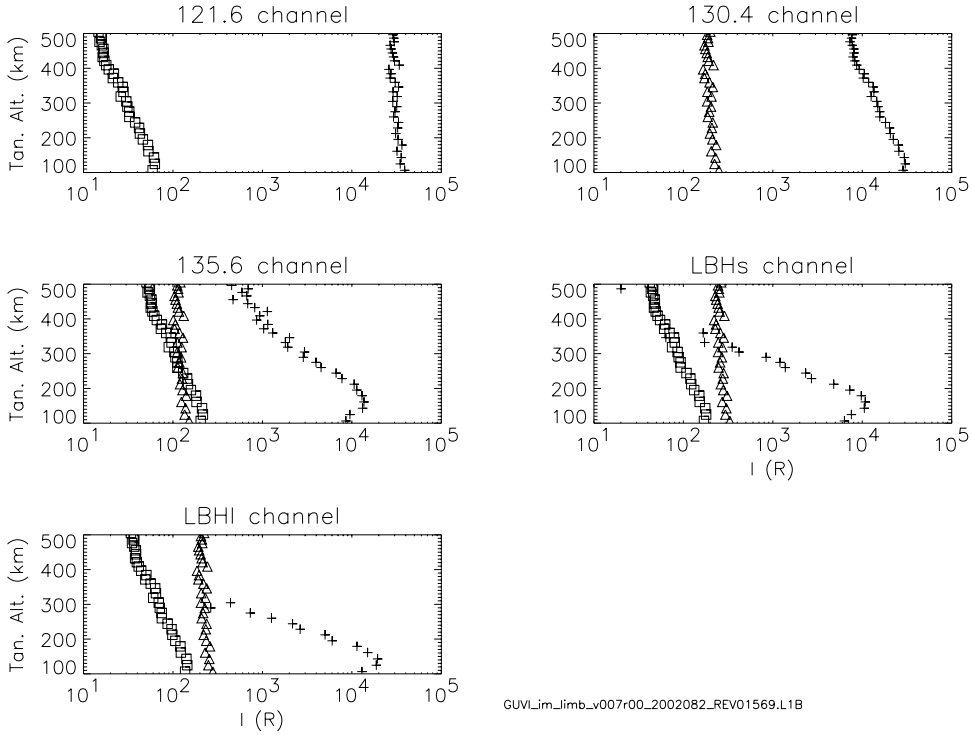

Figure 9. Limb radiances versus tangent altitude. In each panel, a plus symbol indicates the radiance for the channel, triangles indicate the scattered light contribution from Lyman α, and squares indicate the scattered light contribution from OI (130.4). The backgrounds have been removed from the radiances. The solar zenith angle, latitude, and longitude were 32°, −7.9°, and 256°, respectively.

nated by particles associated with the South Atlantic Anomaly (SAA) impacting the instrument. The SAA signature is weaker on day 83 than on day 82.

[20] Both GUVI observations and NRLMSIS model values give approximately hemispherical symmetry in O/N_2 on day 82, although stronger overall latitudinal variations exist in the NRLMSIS results. The symmetry is to be expected since the subsolar point is close to the equator on these days. NRLMSIS also exhibits a longitudinal variation at high latitudes. In both hemispheres, reduced O/N_2 values occur over extended longitude ranges associated with proximity to the magnetic pole and the auroral oval. Auroral heating and its associated circulation reduce O/N_2 within and outside of the heated region. The reduced GUVI O/N_2 values at extreme southern latitudes early in the day (lower right) are likely associated with low-level activity from the previous day.

[21] Significant changes in column O/N_2 occur on day 83 (in both GUVI and NRLMSIS). NRLMSIS exhibits stronger latitudinal and longitudinal variations compared with day 82. The gross longitudinal behavior of O/N_2 seen in NRLMSIS is also present in the GUVI results, along with significant additional structure reflecting regions of reduced O/N_2. These regions arise from nightside transport of heated air from auroral regions to lower latitudes, and the structure of these regions depends critically on when strong heating and associated disturbance winds occur (e.g., see *Craven et al.* [1994] and *Strickland et al.* [2001a, 2001b] and references therein for further details). The O-depleted disturbance over North America is impressive, both in intensity and low-latitude penetration.

[22] A different picture emerges between NRLMSIS and GUVI regarding enhancements in column O/N_2. Low-latitude enhancements of O/N_2 are seen in NRLMSIS at all longitudes. Such enhancements do not appear in this early analysis of GUVI observations, although weak ones occur at various northern locations bordering regions of reduced O/N_2. There is an extended latitudinal region near the left edge of the GUVI image that does show enhancements compared with the previous day. DE-1 observations were also generally lacking in significant enhancements [e.g., *Nicholas et al.*, 1997], but weak enhancements were observed. Additional investigations of this period shall be reported in subsequent papers.

3.2. Dayglow Limb Observations

[23] Detailed information on the altitude distributions of N_2, O, and O_2 is contained in the dayglow limb profiles of the N_2 LBH and OI (135.6) radiances [*Meier and Anderson*, 1983; *Meier and Picone*, 1994]. The emissions are excited by photoelectron impact excitation of N_2 and O. Each column emission rate is related both linearly to the concentrations of the species and nonlinearly through the dependence of the photoelectron flux on atmospheric concentration, as well as through a small multiple scattering component of the OI (135.6) emission. The signature of molecular oxygen is contained in absorption of these emissions below about 160 km tangent altitude (defined as the altitude above the reference geoid where the line-of-sight is perpendicular to the local vertical). Before discussing the retrieval of atmospheric information from limb radiances, we consider typical examples of GUVI limb observations.

[24] A representative single-orbit summary of limb data is presented in Figure 8 constructed by first averaging the 14 "along-track" pixels for a single channel to provide a radiance value at a specific tangent altitude. Radiances from each of the 32 tangent altitudes obtained during the limb segment of the mirror scan were then color-coded according to absolute intensity and stacked vertically to provide a linear image of a single limb scan. Next, each of the 389 limb scans in a TIMED orbit was stacked in time order horizontally to yield a two-dimensional image. The abscissa and ordinate are, respectively, the along-track angle, which measures a full satellite orbital revolution beginning at the ascending node, and the cross track angle, which is related to the tangent altitude (from approximately 100 to 540 km). The upper and lower panel show the O (135.6) and LBHS channels, respectively. The first and last features in the image (along-track angles of 0–5°, 20–40°, and 350–360°) are the nightside tropical radiative recombination emissions coming from the Appleton Anomaly (only visible in the O(135.6) channel). The dominant features in the images (80–260°) are the photoelectron-excited dayglow. The vertical structures around 270° and again at 310° are auroral emissions. For much of the dayglow the vertical variation of emission rate qualitatively follows that expected, reflecting the atomic oxygen scale height on the topside. However, between 170 and 210°, the OI (135.6) emission extends to higher altitudes than elsewhere due to ionospheric radiative recombination (see section 3.4) from the daytime Appleton anomaly. Images such as these are remarkably useful for obtaining a global impression of how the thermosphere varies with height and how that variation changes with solar and geophysical conditions.

[25] The quality of the limb data can be seen in Figure 9, where radiances from all five channels are shown from a single limb scan (taken from Figure 8) at about 180° along-track angle. Two scattered-light contaminants also shown in the figure have been removed from the channel radiances so that except for the highest count rates, the point-to-point variations are not indicative of the counting statistics. The O (135.6) and N2 LBHS channels have sufficiently good statistics for the inversion algorithms, even for the single limb scans shown. As well, successive limb scans overlap successive areas of the sky, so that selective binning of data can improve the signal to noise to an even greater extent. Note that $e + O^+$ radiative recombination emission from the Appleton Anomaly can be seen in the O (130.4) and O (135.6) channels above about 300 km, where the column emission rate scale heights increase.

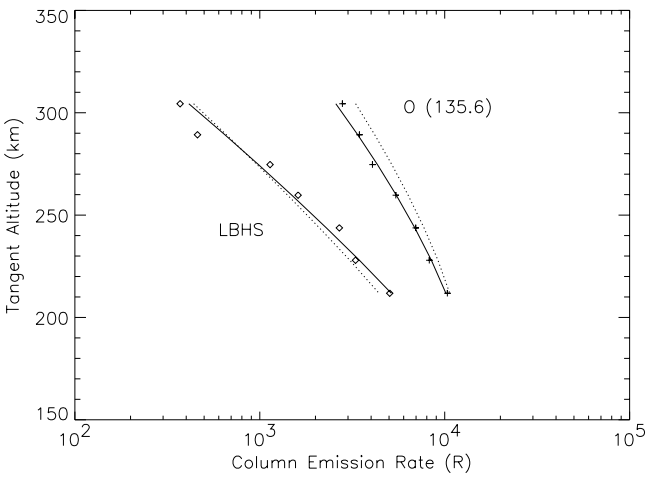

Figure 10. High-altitude limb scan from orbit 1578. At 250 km tangent altitude, the solar zenith angle, latitude, and longitude were 33°, −6.7° and 37.1°, respectively. Plus symbols are for the O (135.6) channel and diamonds are for LBHS. The dotted lines are the initial guess using the NRLMSIS-00 model, and the solid lines are the optimal fits for the retrieved temperatures. Atmospheric concentration was fixed at the NRLMSIS values, but values for the absolute excitation rate were allowed to vary in the retrieval.

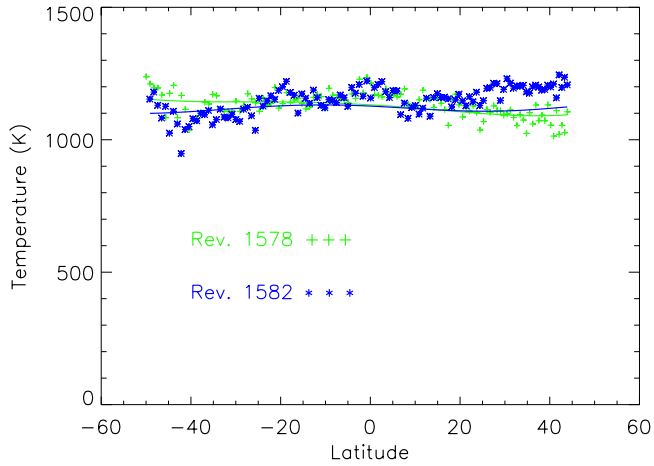

Figure 11. Retrieved daytime exospheric temperatures for magnetically disturbed (1582) (shown by a star) and undisturbed (1578) (shown by a plus symbol) TIMED orbits on 24 March (day 83) 2002. Discrete symbols indicate GUVI temperatures, and solid lines are NRLMSIS-00 predictions. At 40°N, the longitudes for orbits 1578 and 1582 are 15° and 277°, respectively.

[26] The extraction of altitude profiles of the atmospheric composition from radiance data involves a nonlinear inversion procedure. The method we use is commonly called Discrete Inverse Theory (DIT) [*Menke*, 1989]. A forward model of the column emission rates, containing a parameterization of the thermospheric composition and photoelectron g-factors (excitation rate s^{-1} $atom^{-1}$), is combined with the discrete observations of OI (135.6) and N2 LBHS limb radiances to retrieve optimal estimates of the model parameters. Our approach uses the Levenberg-Marquardt method for obtaining the maximum likelihood solution for the model parameters. The parameters consist of three scalar multipliers of the NRLMSISE-00 model [*Picone et al.*, 2002] species concentrations (to establish the magnitudes of the N_2, O, and O_2 concentrations) and one scalar multiplier of the solar 10.7-MHz radio flux (to vary the species altitude profiles). This four-parameter scheme has proven to be stable and robust. *Meier and Picone* [1994] and *Meier et al.* [2001] give more details on the DIT procedures; the latter reference also discusses alternative parameterizations. For inversions of data taken above about 300 km in the tropics, the forward model must include an ionospheric radiative recombination component.

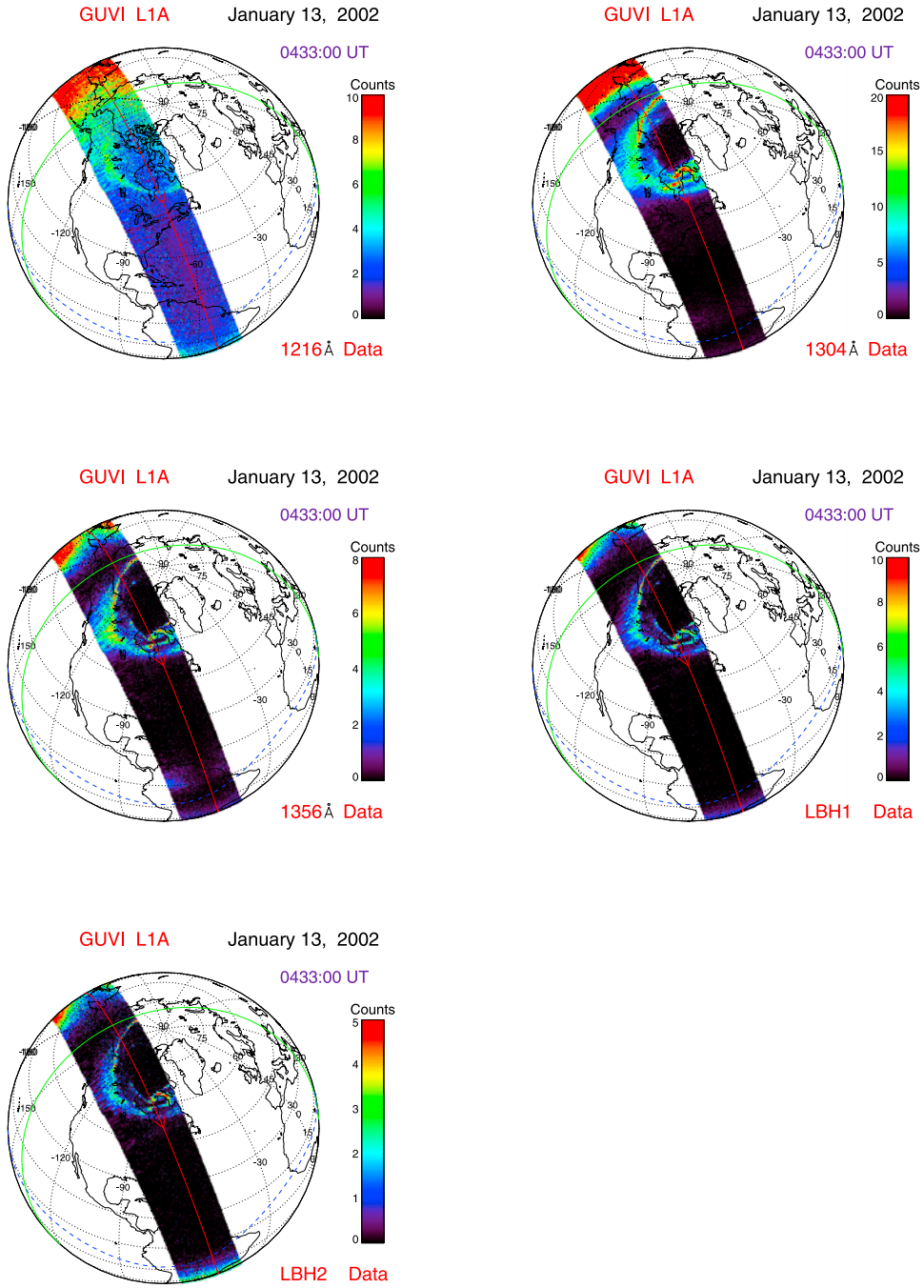

Figure 12. Examples of the aurora and dayglow observed in H(121.6) channel (left panel) and O(135.6) channel (right panel). The two geographic distributions highlight differences in the proton and electron precipitation patterns.

[27] High-quality inversions of limb scan data require that all emission features within the passband of the relevant channels be taken into account. Additionally, proper account must be taken of the instrumental wavelength function for the chosen slit. Observational error budgets must be developed that include systematic and random components. Because pointing errors can be one of the most important drivers of the error budget, special care must be exercised to ensure that all effects have been formally considered. We are currently in the process of addressing these issues and verifying and validating the forward model used in the inversion scheme; consequently, we will not present full limb inversion results in this overview paper. On the other hand, if the inversion method is applied only to data gathered between tangent altitudes of 200–300 km, issues such as pointing uncertainties or ionospheric radiative recombination become minor. At these altitudes, the OI (135.6) (or N_2 LBH) radiances depend linearly on the product of the O (or N_2) line-of-sight column concentration and the absolute value of the excitation rate. At high

altitudes where the emissions are optically thin, uncertainties in these emissions cannot be separated from uncertainties in the instrument calibration, so we cannot retrieve number densities with high accuracy by inverting 200–300 km data. Estimates of exospheric temperature can still be extracted from inversion of the height profiles, however. (We refer to temperatures so obtained as ''estimates'' because they actually do have a composition dependence that is implicit through the dependence of the slope of the g-factors on O and N_2 column density. Ultimate accuracy in obtained temperatures comes with full composition retrievals.)

[28] In section 3.1, we presented disk images of a moderate geomagnetic storm on 24 March (day 83) 2002 that resulted in extensive regional depletions in the column O/N_2 ratio (upper right panel of Figure 7). Using temperature retrievals from limb data, we can determine if the disturbed regions are warmer or cooler than the undisturbed regions. To explore this question, we compare limb profiles for a quiet and a disturbed period. For the quiet period, we invert data from orbit 1598, during which GUVI viewed the undisturbed limb airglow. For the disturbed case, we use orbit 1582, during which GUVI's limb line-of-sight passed through relatively low values of O/N_2 over eastern North America. An example of a single limb scan retrieval from the middle of orbit 1578 is shown in Figure 10. The NRLMSIS-00 model predicted an exospheric temperature of 1137 K corresponding to the radiances shown as dotted lines in Figure 10. The retrieval yielded a value of 1076 ± 21 K. The uncertainty in temperature was computed from the random uncertainties in the observations using standard propagation of errors and does not include uncertainties due to errors in the assumed (NRLMSIS) composition. The DIT-retrieved radiances corresponding to this exospheric temperature are shown as solid lines in Figure 10.

[29] Figure 11 compares full (daytime) orbit temperature retrievals for the quiet (orbit 1578) and disturbed (orbit 1582) passes. During orbit 1582, GUVI viewed the limb in the disturbed atmosphere above eastern North America. The temperatures for the two days were similar in the Southern Hemisphere and at low latitudes. However, beginning at about 20°N, temperatures over North America rose to about 150K greater than those over Europe. The NRLMSIS-00 predictions are similar to the observations in magnitude and hemispherical change, but the climatology cannot capture the structure in the GUVI data. We conclude that the region of low column O/N_2 is hotter than elsewhere. The correlation between high temperatures and depletions is to be expected. Joule heating causes warming and upwelling, and upwelling in turn is the primary cause of depletions under disturbed conditions. Future work will include detailed global temperature and composition retrievals with comparison to thermospheric global circulation models.

3.3. Auroral Precipitation

[30] Auroral emission features are present in all GUVI data channels. Images from two channels obtained during a passage over the Northern Hemispheric aurora on 13 January (day 13) 2002 are shown in Figure 12. HI (121.6) emissions associated with the precipitation of protons are illustrated in Figure 12a, while Figure 12b

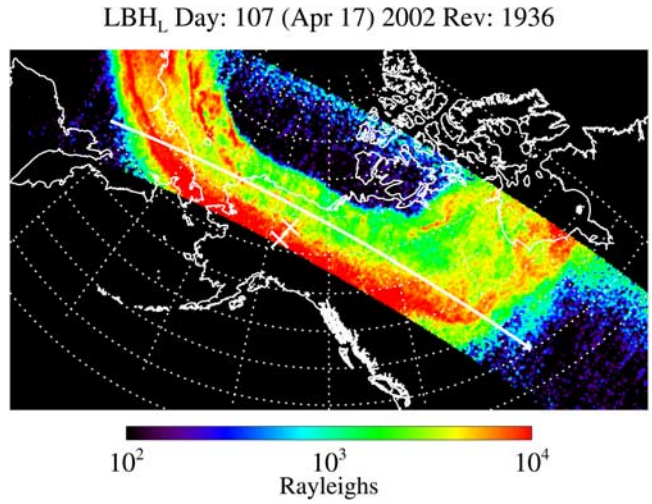

Figure 13. Image data obtained on 17 April (day 107) 2002 using the LBHL channel on GUVI. The white line, at a cross-track look angle of 43°, shows a cut through the image for which data products are presented in Figure 14. The white crosses show the locations of ground-based observatories in central Alaska.

illustrates the corresponding O (135.6) channel image for emissions excited by both protons and energetic electrons. The sunlit atmosphere accounts for the emission in the upper left-hand segment of the images. Subtraction of a dayglow component from the emission (not included in these figures) would allow quantitative measurements of the auroral characteristics under sunlit conditions.

[31] Extraction of a two-parameter representation of the precipitating particle distribution, the total energy flux, Q, and characteristic energy of the distribution, E_o, uses an approach which is a variation on *Strickland et al.* [1989]. It is assumed that the energetic electrons can be represented using either a Gaussian distribution (approximate behavior for discrete aurora) or a Maxwellian distribution (approximate behavior for diffuse aurora).

[32] As discussed by Strickland (submitted reference, 2003), any proton/H-atom aurora that is present has its emission within the O (135.6) and LBH channels assigned to electron precipitation. The observed radiances of the emissions are also dependent on the composition of the neutral atmosphere, thus providing an opportunity to observe composition changes in regions of auroral precipitation. The composition parameter is f_o and represents a multiplicative scaling factor applied to the oxygen density profile in the selected MSIS atmosphere used to construct lookup tables for deriving the data products [*Strickland et al.*, 1989; Strickland, submitted manuscript, 2003].

[33] We have extracted the above three auroral parameters along the white line shown in Figure 13. This radiance map, showing emission within the LBHL channel, is for a pass over North America on 17 April (day 107) 2002. Figure 14 shows Q, E_o, and f_o along the indicated cut from the previous figure. The applied lookup table was constructed from auroral electron transport calculations for which electron precipitation was characterized by Gaussian distribu-

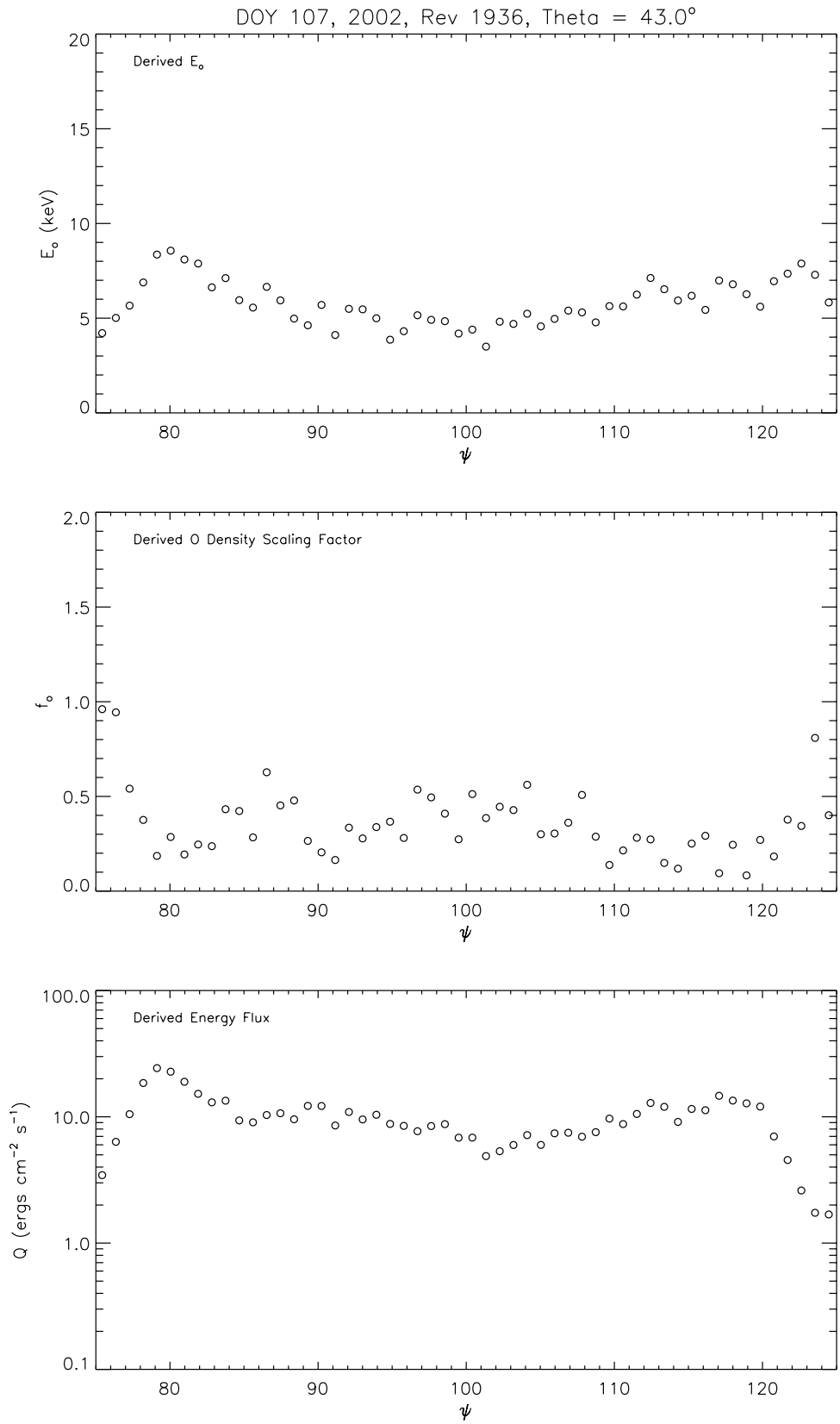

Figure 14. Values of the auroral parameters, E_o, f_o, and Q derived from observations along the satellite track (43° off-track look angle) shown in Figure 13. The abscissa is the angle along the orbit measured from the ascending node (northbound equator crossing). In this case, 100 degrees corresponds approximately to central Alaska.

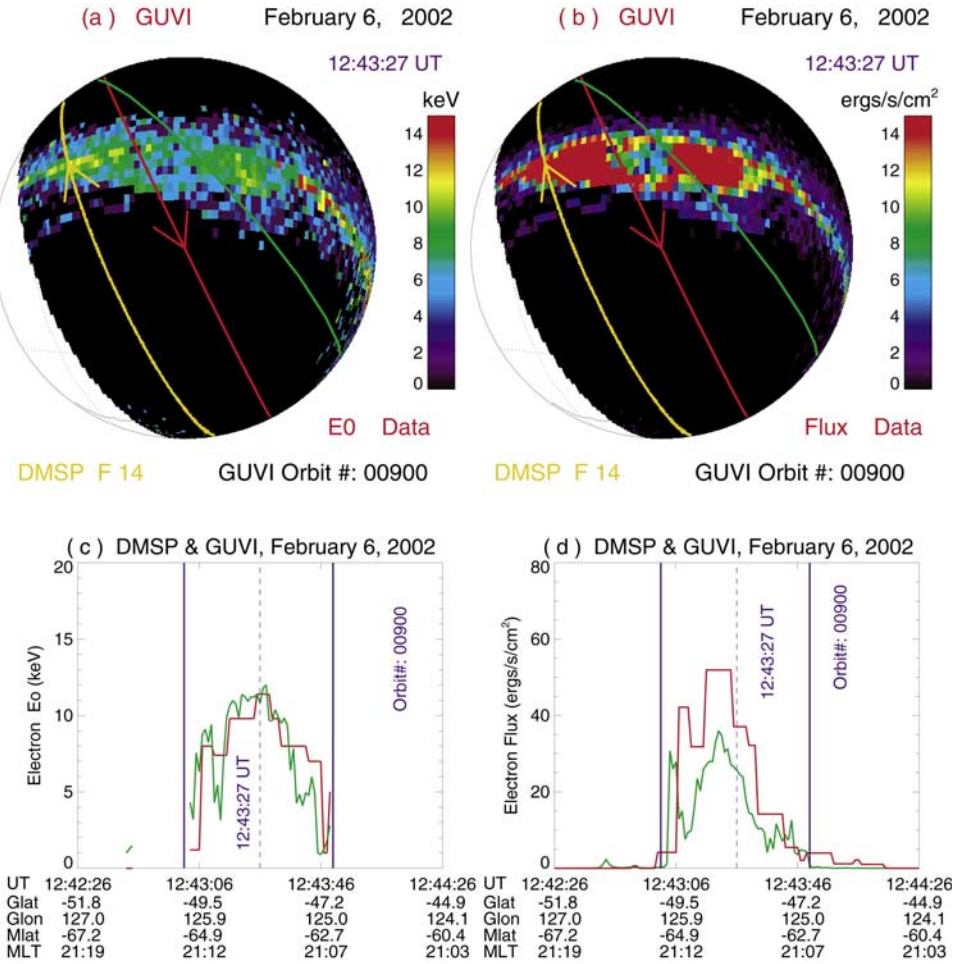

Figure 15. Maps of auroral electron characteristic energy (a) and energy flux (b) estimated from GUVI data and profiles of the characteristic energy (c) and energy flux (d) along the DMSP F14 path between1242:26 and 1244:26 UT, 6 February (day 37) 2002 for both GUVI (red) and DMSP (green). The yellow, red, and green lines are for the DMSP F14 orbit, TIMED orbit, and the ground terminator at 1243:27 UT, respectively. The yellow and red arrows indicate the DMSP and TIMED location at 1243:27 UT. The curves in Figure 15c were plotted only for the DMSP electron energy fluxes above 1.0 ergs/s/cm^2.

tions. The auroral energy flux Q was consistent with a Class II aurora (approximately 10 ergs/cm^2/s), and E_o was approximately 5 kev. The neutral atmosphere appears to have been poor in atomic oxygen with $f_o \leq 0.5$.

[34] An initial comparison between the electron flux and characteristic-energy estimates from GUVI and those measured with the SSJ particle detector on an Air Force DMSP satellite are shown in Figure 15. Note that the aurora at the point of interest is sunlit, thereby requiring additional steps in the processing to remove the dayglow contribution to the measured radiances.

[35] The lower-left panel compares E_o derived from GUVI with that from SSJ on DMSP. Some of the spatial variability that was captured by the DMSP sensor is not evident in the GUVI results, however the magnitudes are in excellent agreement. As for Q, there is a greater degree of offset in the results. At the peak the GUVI result exceeds the DMSP by about 40%. This difference could easily be due to the temporal offset of the measurements, approximately 4 min. Clearly, additional measurements will be needed to fully validate the GUVI processing, but as an initial experiment it has given us much confidence in the analysis approach.

3.4. Ionospheric Signatures

[36] Although investigations of ionospheric phenomena were considered a secondary objective of the TIMED mission, the GUVI observations appear to hold great potential for the study of major ionospheric processes associated with the Appleton Anomaly region. The F-region equatorial Appleton anomalies are bands of enhanced plasma density with maximum densities located about ±15° on either side of the magnetic dip equator. These regions are the result of $\mathbf{E} \times \mathbf{B}$ forcing that transports plasma from the equatorial ionosphere to higher altitudes and latitudes creating a fountain effect in the plasma flow [*Moffett and Hanson*, 1965]. This phenomenon has been extensively studied and continues to be an active topic of research because of the association with strong effects on the propagation of radio and GPS signals [cf. *Moffett*, 1979;

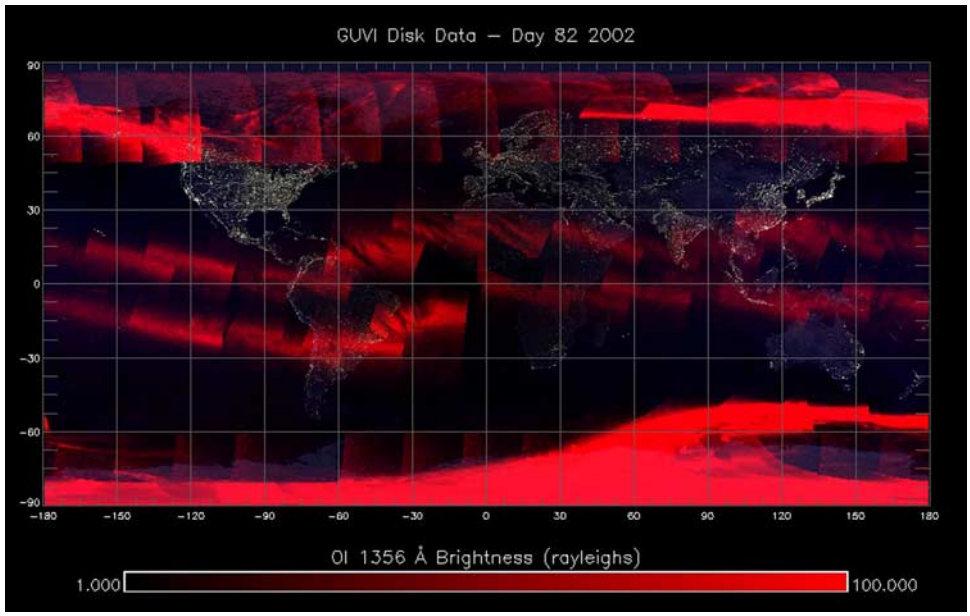

Figure 16. O (135.6) channel night-side disk images for 23 March (day 82) 2002. This is a composite image of successive nightside passes. The bands of emission that parallel the geomagnetic equator are FUV emission associated with the Appleton ionospheric anomalies. The color scale is linear and indicates the brightness in Rayleighs. The feature on the southeastern coast of South America including parts of Brazil and Argentina is due to particle contamination in the south Atlantic magnetic anomaly.

Anderson, 1973; *Abdu et al.*, 1990; *Klobuchar et al.*, 1991; *Whalen*, 1998].

[37] A distinct but related phenomenon is the formation of so-called plasma bubbles in the evening sector of the lower F-region. The bubbles produce a signature (range spread) in vertical ionograms called equatorial spread-F [*Cohen and Bowles*, 1961]. The range spread is caused by the irregularities in the spatial distribution of plasma. The properties of spread-F can also be investigated using incoherent scattering of radio waves [*Woodman and La Hoz*, 1976]. The bubbles of depleted plasma rise vertically and drift easterly and appear to be triggered by atmospheric gravity waves [*Kelley et al.*, 1981].

[38] In the Appleton anomalies, the high ionospheric ion densities give rise to FUV radiative recombination emission [*Hanson*, 1969]. The brightness of the emission varies as the product of the electron density and the oxygen ion concentration. Since in the F region, these quantities are approximately equal, the OI (135.6) emission follows the square of the electron density [cf. *Meier*, 1991]. For the OI

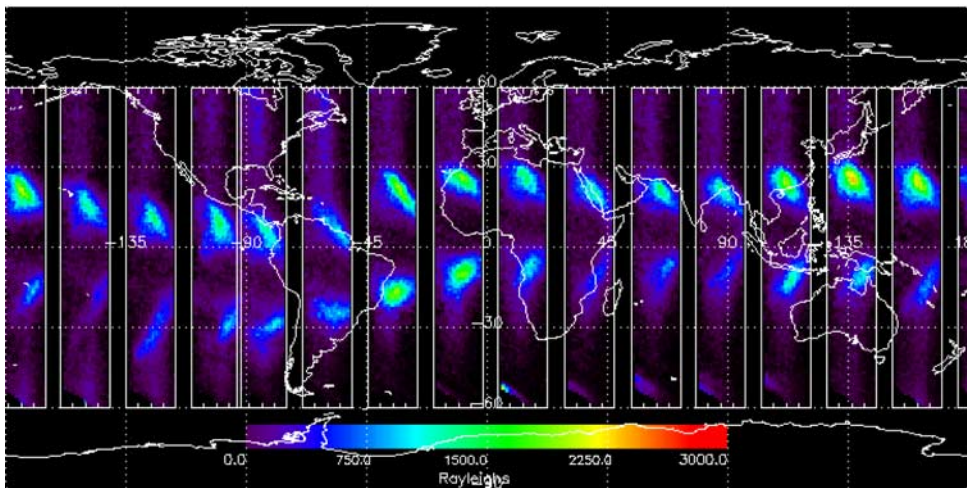

Figure 17. O (135.6) channel limb scans of the nightside ionosphere in successive orbits on 15 February (day 46) 2002. The equatorial crossing time was approximately 1830 LT. The data on successive orbits are laid out with latitude in the vertical and tangent altitude in the horizontal direction. Each box is placed on the map such that its center corresponds to the location of the point at which the GUVI line-of-sight crosses the equator at a tangent altitude of 320 km.

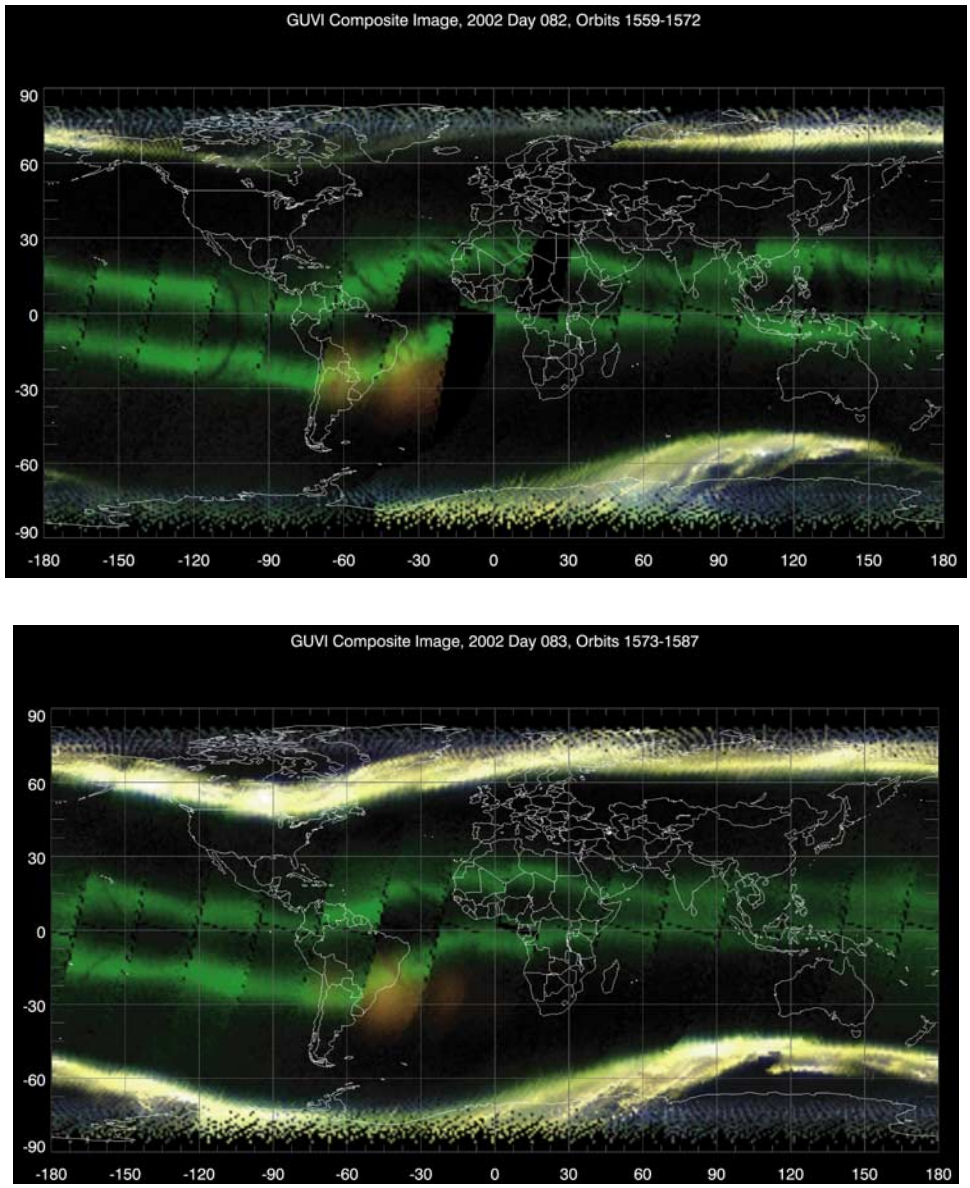

Figure 18. An RGB (LBHS, O (135.6), and H (121.6), respectively) representation of the GUVI nightside data for 23 March 2002 (day 82) (left panel) and 24 March 2002 (day 83) (right panel). This composite image shows the nightside ionosphere due to the recombination of O+ and electrons which produces a signal in the O (135.6) channel (green). The equatorial fountain effect produces the arcs (seen as green bands) on either side of the magnetic equator. The dark streaks and arcs seen against the bright green background represent areas of local ionospheric depletions. Radiation induced counts from the South Atlantic Anomaly (SAA) only appear in the LBHS channel due to lower responsivity in the channel and is seen as a reddish tint. This indictates that even as the TIMED spacecraft passes through this region of enhanced energetic particles, GUVI is still able to clearly image small-scale ionospheric irregularities. The strong white bands at the top and bottom of the image indicate the presence of aurora which saturates the color table in all three channels in this representation.

(130.4) and to a much lesser extent for OI (135.6) corrections for resonance scattering must be applied. There is also is a small contribution to the emission from $O^+ + O^- \rightarrow 2O$ mutual neutralization. Hence in the GUVI images to follow, the radiance can be regarded as an approximate map of the square of the electron concentration at the peak of the F region.

[39] Nightside swaths of the O (135.6) channel obtained in the disk-imaging mode are shown in Figure 16 for a full day's orbits. The red line denotes the start of the day and the orbits proceed from right to left. Since the LBH bands are not generated by recombination, the emission is purely atomic oxygen in this channel. These images show the anomaly at the same local time but for different longitudes and universal times in each successive orbit. Within each swath, the signal is brightest near the edges of the scans due to the longer path length through the ionosphere at large off-nadir angles. North-south asymmetries are clearly evident in

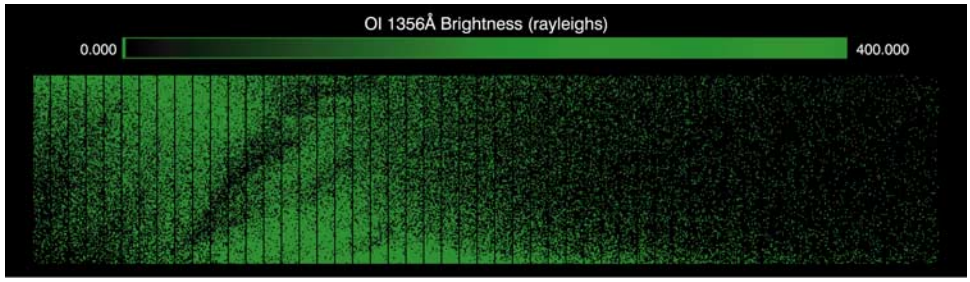

Figure 19. An expanded view of an ionospheric bubble within the Appleton Anomaly. The vertical lines delineate individual scans of the GUVI mirror. The width of the each scan is given by the 14 pixels along the length of the GUVI slit. At the height of the F region assumed to be approximately 350 km, the slit projection spans approximately 50 km.

all swaths. Meridional winds are known to redistribute the ions that are raised to higher altitudes near the dip equator by ionospheric electric fields [*Anderson*, 1973; *Abdu et al.*, 1990; *Venkatraman and Heelis*, 2000]. The radiance of the OI (135.6) reaches approximately 10R in this figure. A Chapman layer with a peak electron density of 2×10^6 electrons/cm^3 would give an equivalent radiance.

[40] Observations of the vertical and horizontal structure within the Appleton anomaly are illustrated in Figure 17. Here are shown the limb scan data for each nightside orbital pass over the course of a full day. During each pass of the satellite, limb scans are obtained with each scan of the mirror (15 s). These limb scans illustrate the ion distribution in altitude and latitude. The altitude of the peak ion density tends to rise and the concentration tends to fall as one moves toward the equator in accordance with distribution expected from the fountain effect.

[41] An alternate representation of nightside images is shown in Figure 18 where red, green, and blue colors are scaled by the LBHS, O (135.6), and H (121.6) channel radiances, respectively. The images illustrate the day-to-day variability of the Appleton anomaly and show the appearance of narrow, often curved, depleted (dark) regions associated with "plasma bubbles." These regions of reduced ion concentration in equatorial plasma bubbles cause a reduced recombination emission [*Paxton et al.*, 2002]. The depletions appear as sharp drops in the ion density measured by orbiting satellites [*Huang et al.*, 2001]. However, the data shown in the right hand panel of Figure 18 are a dramatic example of the power of the GUVI instrument to address the large-scale characteristics of the bubble processes. An expanded view of a bubble structure is shown in Figure 19. The depletions are approximately 50–100 km in width and extend several hundred kilometers in length.

4. Conclusions

[42] The GUVI investigation is providing accurate and reliable global measurements of the composition, temperature, and density of the thermosphere and ionosphere and the aurora. Such measurements are essential to improve our understanding of the state of the upper atmosphere and its response to solar and geomagnetic forcing. The GUVI data are particularly useful in that they provide instantaneous altitude profiles of various geophysical parameters, rather than the simple point measurements obtained by in situ sampling. In particular, the imaging character of GUVI allows tracking of the evolution of magnetic storm-induced perturbations of the atmosphere. Validation of global thermospheric-ionospheric global circulation models has been seriously hampered by the lack of systematic temperature, composition, and ion number density data. GUVI will provide an important contribution to the needed data.

[43] The set of observations and initial analyses presented herein demonstrate the value of the GUVI instrument for the study of the thermosphere and ionosphere. Validation activities have demonstrated the nominal performance of the GUVI instrument. We have a growing degree of confidence in the validity of measurements for the column O/N_2 ratio, thermospheric temperature, and auroral parameters and expect that additional studies will confirm the accuracy and precision of the GUVI results, including retrieval of altitude profiles of composition. We believe that GUVI has already proven and will continue to show that remote sensing of the thermosphere and ionosphere has come of age. We expect that FUV imaging will have an impact on space weather monitoring analogous to that had by visible and infrared imaging on tropospheric weather.

[44] **Acknowledgments.** The GUVI team wishes to acknowledge the engineering and software support from Michele Weiss, Bill Wood, Jim Eichert, John Goldsten, Bill Crain, Dan Mabry, and Patty Lew. We wish to acknowledge NASA grant NAG5-5001 to The Aerospace Corporation for partial support of this project.

[45] Arthur Richmond thanks D. McEwen and Stanley Solomon for their assistance in evaluating this paper.

References

Abdu, M. A., G. O. Walker, B. M. Reddy, J. H. Sobral, B. G. Fejer, T. Kikuchi, N. B. Trivedi, and E. P. Szuszczewicz, Electric field versus neutral wind control of the equatorial anomaly under quiet and disturbed conditions: A global perspective from SUNDIAL 86, *Ann. Geophys.*, *8*, 419–430, 1990.

Ajello, J. M., and D. E. Shemansky, A re-examination of important N_2 cross section by electron impact with application to the dayglow: The Lyman-Birge-Hopfield band system and NI (119.99 nm), *J. Geophys. Res.*, *90*, 9845, 1985.

Anderson, D. N., A theoretical study of the ionospheric F-region equatorial anomaly, I, Theory, *Planet. Space Sci.*, *21*, 409–419, 1973.

Christensen, A. B., et al., The Global Ultraviolet Imager (GUVI) for the NASA TIMED mission, in *Optical Spectroscopic Techniques and Instrumentation for Atmospheric and Space Research*, vol. 2266, p. 451, Soc. of Photo-Optical Instrum. Eng., Bellingham, Wash., 1994.

Cohen, R., and K. L. Bowles, On the nature of equatorial spread F, *J. Geophys. Res.*, *66*, 1081–1106, 1961.

Craven, J. D., A. C. Nicholas, L. A. Frank, D. J. Strickland, and T. J. Immel, Variations in FUV dayglow after intense auroral activity, *Geophys. Res. Lett.*, *21*, 2793–2796, 1994.

Dymond, K. F., S. E. Thonnard, R. P. McCoy, and R. J. Thomas, An optical remote sensing technique for determining nighttime F-region electron density, *Radio Sci.*, *32*, 1985, 1997.

Eastes, R. W., Modeling the N_2 Lyman-Birge-Hopfield bands in the dayglow: Including radiative and collisional cascading between the singlet states, *J. Geophys. Res.*, *105*, 18,557, 2000.

Eastes, R. W., P. D. Feldman, E. P. Gentieu, and A. B. Christensen, The ultraviolet dayglow at solar maximum. I. FUV spectroscopy at 3.5 A resolution, *J. Geophys. Res.*, *90*, 6594, 1985.

Feldman, P. D., and E. P. Gentieu, The ultraviolet spectrum of an aurora 530–1520 A, *J. Geophys. Res.*, *87*, 2453, 1982.

Germany, G. A., D. G. Torr, P. G. Richards, M. R. Torr, and S. John, Determination of ionospheric conductivities from FUV auroral emissions, *J. Geophys. Res.*, *99*, 23,297–23,305, 1994.

Goldsten, J. O., D. C. Humm, L. J. Paxton, B. S. Ogorzalek, S. A. Gary, J. R. Hayes, and J. D. Boldt, Performance of the wedge-and-strip microchannel plate detectors and electronics for the global ultraviolet imager (GUVI), *SPIE EUV X-Ray Gamma-Ray Instrum. Astron.*, *3765*, 408–416, 1999.

Hanson, W. B., Radiative recombination of atomic oxygen ions in the nighttime F- region, *J. Geophys. Res.*, *74*, 3720, 1969.

Huang, C. Y., W. J. Burke, J. S. Machuzak, L. C. Gentile, and P. J. Sultan, DMSP observations of equatorial plasma bubbles in the topside ionosphere near solar maximum, *J. Geophys. Res.*, *106*, 8131–8142, 2001.

Huffman, R. E., F. J. LeBlanc, J. C. Larrabee, and D. E. Paulsen, Satellite vacuum ultraviolet airglow and auroral observations, *J. Geophys. Res.*, *85*, 2201, 1980.

Humm, D. C., et al., Design and performance of the Global Ultraviolet Imager (GUVI), *Proc SPIE X-Ray Gamma-Ray Instrum. Astron.*, *3445*, 2–12, 1998.

Humm, D. C., B. S. Ogorzalek, M. J. Elko, D. Morrison, and L. J. Paxton, Optical calibration of the Global Ultraviolet Imager (GUVI), *SPIE Ultraviolet Atmos. Space Remote Sens. Method. Instrum.*, *3818*, 78–89, 1999.

Immel, T. J., G. Crowley, J. D. Craven, and R. G. Roble, Dayside enhancements of thermospheric O/N_2 following magnetic storm onset, *J. Geophys. Res.*, *106*, 15,471–15,488, 2001.

Kelley, M. C., M. F. Larsen, C. La Hoz, and J. P. McClure, Gravity wave initiation of equatorial spread F: A case study, *J. Geophys. Res.*, *86*, 9087–9100, 1981.

Killeen, T. L., et al., TIMED Doppler Interferometer (TIDI), *SPIE Proc.*, *3756*, 289–301, 1999.

Klobuchar, J. A., D. N. Anderson, and P. H. Doherty, Model studies of the latitudinal extent of the equatorial anomaly during equinoctial conditions, *Radio Sci.*, *26*, 1025–1047, 1991.

Lummerzheim, D., M. H. Rees, D. J. Craven, and L. A. Frank, Ionospheric Conductances Derived from DE-1 Auroral Images, *J. Atmos. Terr. Phys.*, *53*, 281, 1991.

Martin, C. P., P. Jelinsky, M. Lampton, R. F. Malina, and H. O. Anger, Wedge-and-strip anodes for centroid-finding position-sensitive photon and particle detectors, *Rev. Sci. Instrum.*, *52*, 1067–1074, 1981.

Meier, R. R., Ultraviolet spectroscopy and remote sensing of the upper atmosphere, *Space Sci. Rev.*, *58*, 1–186, 1991.

Meier, R. R., and D. E. Anderson Jr., Determination of atmospheric composition and temperature from the UV airglow, *Planet Space Sci.*, *31*, 967, 1983.

Meier, R. R., and J. M. Picone, Retrieval of absolute thermospheric concentrations from the far UV dayglow: An application of discrete inverse theory, *J. Geophys. Res.*, *99*, 6307, 1994.

Meier, R. R., R. R. Conway, D. E. Anderson Jr., P. D. Feldman, R. W. Eastes, E. P. Gentieu, and A. B. Christensen, The ultraviolet dayglow at solar maximum 3. Photoelectron-excited emissions of N_2 and O, *J. Geophys. Res.*, *90*, 6608, 1985.

Meier, R. R., J. M. Picone, D. P. Drob, and R. Roble, Similarity transformation-based analysis of atmospheric models, data, and inverse remote sensing algorithms, *J. Geophys. Res.*, *106*, 15,519–15,532, 2001.

Menke, W., *Geophysical Data Analysis: Discrete Inverse Theory*, *Int. Geophys. Ser.*, vol. 45, Academic, San Diego, Calif., 1989.

Moffett, R. J., The equatorial anomaly in the electron distribution of the terrestrial F region, *Fund. Cosmic Phys.*, *4*, 313–391, 1979.

Moffett, R. J., and W. B. Hanson, Effect of ionization transport on the equatorial F-region, *Nature*, *206*, 705, 1965.

Morrison, D., L. J. Paxton, H. Kil, Y. Zhang, B. S. Ogorzalek, and C.-I. Meng, On-orbit calibration of the Special Sensor Ultraviolet Scanning Imager (SSUSI): A far-UV imaging spectrograph on DMSP F-16, *SPIE Opt. Spectrosc. Tech. Instrum. Atmos. Space Res.*, *4485*, 328–337, 2002.

Nicholas, A. C., J. D. Craven, and L. A. Frank, A survey of large-scale variations in the thermospheric oxygen column density with magnetic activity as inferred from observations of the FUV dayglow, *J. Geophys. Res.*, *102*, 4493–4510, 1997.

Paxton, L. J., C.-I. Meng, G. H. Fountain, B. S. Ogorzalek, E. H. Darlington, J. Goldstein, and K. Peacock, SSUSI: Horizon-to-horizon and limb viewing spectrographic imager for remote sensing of environmental parameters, *Ultraviolet Technol.*, *1764*, 161–176, 1992a.

Paxton, L. J., C. I. Meng, G. H. Fountain, B. S. Ogorzalek, E. H. Darlington, J. Goldsten, S. Geary, D. Kusnierkiewicz, S. C. Lee, and K. Peacock, Special Sensor UV Spectrographic Imager (SSUSI): An instrument description, *Instrum. Planet. Terr. Atmos. Remote Sens.*, *1745*, 2–16, 1992b.

Paxton, L. J., D. J. Strickland, M. Weiss, and C.-I. Meng, Interactive data analysis and display of far ultraviolet data, *COSPAR Adv. Space Res.*, *22*(11), 1577–1582, 1998.

Paxton, L. J., et al., Global ultraviolet imager (GUVI): Measuring composition and energy inputs for the NASA Thermosphere Ionosphere Mesosphere Energetics and Dynamics (TIMED) mission, *Proc. SPIE*, *3756*, 265–276, 1999.

Paxton, L. J., D. Morrison, H. Kil, Y. Zhang, B. S. Ogorzalek, and C. Meng, Validation of remote sensing products produced by the Special Sensor Ultraviolet Scanning Imager (SSUSI): A far UV imaging spectrograph on DMSP F-16, *SPIE Opt. Spectrosc. Tech. Instrum. Atmos. Space Res.*, *4485*, 338–348, 2002.

Picone, J. M., A. E. Hedin, D. P. Drob, and A. C. Aikin, NRLMSISE-00 empirical model of the atmosphere: Statistical comparisons and scientific issues, *J. Geophys. Res.*, *107*(A12), 1468, doi:10.1029/2002JA009430, 2002.

Russell, J. M., III, M. G. Mlynczak, L. L. Gordley, J. Tansock, and R. Esplin, An overview of the SABER experiment and preliminary calibration results, *SPIE Proc.*, *3756*, 277–288, 1999.

Strickland, D. J., and G. E. Thomas, Global atomic oxygen density derived from OGO-6 1304 A airglow measurements, *Planet. Space Sci.*, *24*, 313, 1976.

Strickland, D. J., J. R. Jasperse, and J. A. Whalen, Dependence of auroral FUV emissions on the incident electron spectrum and neutral atmosphere, *J. Geophys. Res.*, *88*, 8051, 1983.

Strickland, D. J., R. R. Meier, J. H. Hecht, and A. B. Christensen, Deducing composition and incident electron spectra from ground-based auroral optical measurements: Theory and model results, *J. Geophys. Res.*, *94*, 13,527, 1989.

Strickland, D. J., J. S. Evans, and L. J. Paxton, Satellite remote sensing of thermospheric O/N_2 and solar EUV: 1. Theory, *J. Geophys. Res.*, *100*, 12,217, 1995.

Strickland, D. J., R. E. Daniell, and J. D. Craven, Negative ionospheric storm coincident with DE-1 observed thermospheric disturbance on October 14, 1981, *J. Geophys. Res*, *106*, 21,049, 2001a.

Strickland, D. J., J. D. Craven, and R. E. Daniell, Six days of thermospheric/ionospheric weather over the Northern Hemisphere in late September 1981, *J. Geophys. Res*, *106*, 30,291, 1981.

Venkatraman, S., and R. Heelis, Interhemispheric plasma flows in the equatorial topside ionosphere, *J. Geophys. Res.*, *105*, 18,457–18,464, 2000.

Whalen, J. A., Appleton anomaly increase following sunset: Its observed relation to equatorial F layer $\mathbf{E} \times \mathbf{B}$ drift velocity, *J. Geophys. Res.*, *103*, 9497–9503, 1998.

Woodman, R. F., and C. La Hoz, Radar observations of F region equatorial irregularities, *J. Geophys. Res.*, *81*, 5447–5466, 1976.

Woods, T. N., F. G. Eparvier, S. M. Bailey, S. C. Solomon, G. J. Rottman, G. M. Lawrence, R. G. Roble, O. R. White, J. Lean, and W. K. Tobiska, TIMED solar EUV experiment, *SPIE Proc.*, *3442*, 180–191, 1998.

S. Avery, University of Colorado, Boulder, CO 80309, USA. (susan.avery@colorado.edu)

J. Craven, University of Alaska, Fairbanks, AK 99775, USA. (craven@gi.alaska.edu)

A. B. Christensen, P. Straus, and R. L. Walterscheid, Space Science Applications Laboratory, Aerospace Corporation, El Segundo, CA 90245, USA. (andrew.b.christensen@aero.org; paul.strauss@aero.org; richard.w.walterscheid@aero.org)

G. Crowley, Southwest Research Institute, San Antonio, TX 78238, USA. (gcrowley@swri.edu)

D. C. Humm, H. Kil, C.-I. Meng, D. Morrison, B. X. Ogorzalek, L. J. Paxton, B. Wolven, and Y. Zhang, Applied Physics Laboratory, Johns Hopkins University, Laurel, MD 20723, USA. (david.humm@jhuapl.edu; hyosub.kil@jhuapl.edu; ching.meng@jhuapl.edu; danniel.morrison@jhuapl.edu; bernie.ogorzalek@jhuapl.edu; brian.wolven@jhuapl.edu; yongliang.zhang@jhuapl.edu)

R. R. Meier, E. O. Hulbert Center for Space Research, Naval Research Laboratory, Washington, D. C., 20375, USA. (meier@uap2.nrl.navy.mil)

D. J. Strickland, Computational Physics, Inc., Springfield, VA 22151, USA. (dstrick@cpi.com)

R. M. Swenson, Utah State University, Logan, UT 84322, USA. (charles.swenson@usu.edu)